Electronic transport across linear defects in graphene

C. J. Páez* and A. L. C. Pereira
Faculdade de Ciências Aplicadas, Universidade Estadual de Campinas, 13484-350 Limeira, SP Brazil

J. N. B. Rodrigues
Centre for Advanced 2D Materials, Faculty of Science, National University of Singapore, 6 Science Drive 2, Singapore 117546

N. M. R. Peres
Centro de Física e Departamento de Física, Universidade do Minho, P-4710-057, Braga, Portugal
(Received 2 April 2015; revised manuscript received 28 May 2015; published 24 July 2015)

We investigate the low-energy electronic transport across grain boundaries in graphene ribbons and infinite flakes employing two distinct techniques. Using the recursive Green's-function method, we compute the electronic transmittance across different types of grain boundaries in graphene ribbons and flakes. We use the charge and current density spatial distributions to enhance our understanding of their electronic transport properties. We find that electronic transport depends both on the grain boundaries' microscopic details and on their orientation. In addition, we employ the transfer-matrix formalism to analytically study the electronic transport across a class of zigzag grain boundaries with periodicity 3. We find that these grain boundaries give rise to intervalley scattering.

DOI: 10.1103/PhysRevB.92.045426 PACS number(s): 73.63.−b, 81.05.ue

I. INTRODUCTION

The synthesis of graphene by chemical vapor deposition (CVD) on metal surfaces is the most widely used method for producing graphene sheets [1–4]. CVD graphene, as any other solid grown by CVD, is especially prone to the formation of grain boundaries (GBs) and extended defect lines, which hinder its electronic properties [5–9].

Graphene is being proposed for a variety of new electronic devices [10,11]. However, the required high-quality electrical properties are affected by the formation of polycrystalline structures [12–15]. These structures are practically unavoidable by the growth methods known so far [7,8]. As such, the scattering problem of an electron off a grain boundary (GB) becomes a theoretically and experimentally relevant one [16–20].

The sp^2 bonding structure of carbon atoms in graphene gives rise to extended topological defects that are typically composed of pentagonal, heptagonal, and octagonal rings of carbon atoms, together with distorted hexagons [5–8]. GBs are in general neither perfectly straight lines nor periodic, intercepting each other at random angles. However, periodic straight GBs and defect lines can also be observed in graphene [6], and more interestingly they can be controllably synthesized at precise locations and orientations [13,21], lifting the prospects for the engineering of arrays of such defects that would allow us to manipulate the electronic valley degree of freedom in graphene.

GBs are known to strongly influence the properties of graphene, namely its chemical, mechanical, and electronic ones [22–26]. GBs are expected to present different degrees of transparency to electron transport, depending on their microscopic details and on the relative orientations of the grains separated by them [16,18,19,25,27,28]. In fact, measurements of electronic mobilities of different CVD samples have shown that their electronic properties strongly depend on the details of the CVD-growth recipes [1,2,4,7]. Interestingly enough, and of direct relevance to our work, recent research has probed the electric properties of single GBs [12,29,30].

In a revealing work, Yazyev *et al.* [25] have studied electronic scattering from a wide variety of periodic GBs. In that work, based on momentum conservation along the periodic grain boundary, the authors have shed light on whether low-energy electrons traveling from one grain to the other may feel a transport gap at the GB. Their conclusions were also quantitatively corroborated by first-principles quantum transport calculations (based on density functional theory and the nonequilibrium Green's-function formalism).

Our approach to the scattering problem due to GB's follows two different routes. In the first route we use the recursive Green's-function method to numerically calculate the transmission through defect lines in graphene ribbons. We map charge density over each sublattice site and also the current density through the defects. Following the experiments [12–14], we consider grain boundaries composed of extended linear defects of type 585 (pentagons and octagons) and 5757 (pentagons and heptagons) aligned perpendicular to the ribbon longitudinal direction. Our results for the resistance across a linear defect, i.e., $R \propto 1/\sqrt{V_g}$, compare well with recent experimental results [12] not too close to the Dirac point ($V_g \approx 0$). Close to vanishing charge-carrier density, the electron-hole puddles dominate the physics and thus, since our calculations ignore charge-carrier fluctuations, the deviation from experimental observations is natural. Furthermore, we find strong dependence of the electronic transport properties of such systems with the grain boundaries' orientation in the ribbon. We also consider graphene flakes with bilayer GBs: a spatial region where the grain boundary is composed by the superposition of two monolayer domains, as shown in Fig. 1. For this kind of overlapping bilayer boundary, previous results have already shown interesting conductance oscillations [31]. Here we shed light on these results by analyzing the spatial

*Corresponding author: carlos.gonzalez@fca.unicamp.br

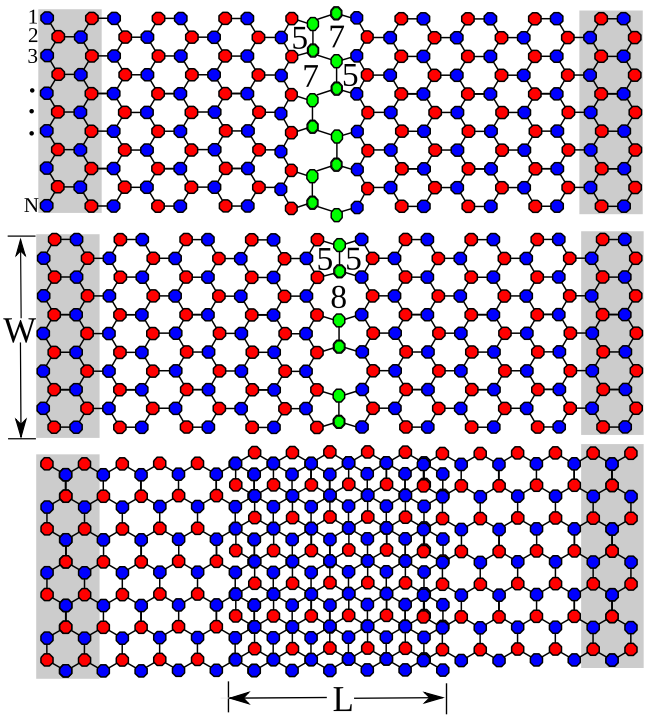

FIG. 1. (Color online) Schematic representation of the different linear defect structures considered as grain boundaries. On the top is the 5757 structure. In the middle we show the 585 linear defect. At bottom is the bilayer graphene of length L, formed by the overlap of two monolayer regions. The shadow areas represent the left and right semi-infinite contacts.

map of the current and the charge density distribution in these overlapped regions.

In the second route, we concentrate on a particular class of grain boundaries briefly addressed by Yazyev *et al.*, namely, those with periodicities such that both Dirac points (at each side of the grain boundary) are mapped into the Γ point of the projected Brillouin zone. In such cases, intervalley scattering of massless Dirac fermions is allowed at the grain boundary. We have chosen to investigate zigzag aligned periodic linear defects separating two grains with the same orientation (also referred to in the literature as degenerate, i.e., zero misorientation angle, grain boundaries). Several such defect lines were proposed in the context of *ab initio* works both on graphene and on boron nitride: the $t7t5$ defect line [32] and the 7557 defect line [33] (see Fig. 8) are two examples. In the context of graphene's single-particle first-neighbor tight-binding model, we use the transfer-matrix formalism to analytically compute the transmittance of electrons across these defect lines, following the methodology developed for the cases of the pentagon-only, $zz(558)$, and $zz(5757)$ defect lines [18,19]. We will show that the boundary condition seen by the electrons at the GB (controlling the electronic scattering) is strongly determined by the GBs' microscopic tight-binding parameters. Furthermore, we will see that these boundary conditions explicitly introduce intervalley scattering. Therefore, these grain boundaries can thus be regarded as a useful nanostructure for valleytronics circuits.

In Sec. II we briefly introduce the reader to the recursive Green's-function method used in Secs. III–V. Section III is devoted to investigate the electronic transport in an armchair ribbon with a GB oriented perpendicularly to its longitudinal direction. In Sec. IV we study the dependence of the electronic transport in a ribbon with the GB orientation. Section V examines the electronic transport properties of an overlap between two semi-infinite monolayer graphene regions. In Sec. VI we make use of the transfer-matrix formalism to investigate zigzag aligned grain boundaries with periodicity 3, concluding the paper with a brief summary of the results obtained—see Sec. VII.

II. TIGHT-BINDING MODEL AND TRANSPORT FORMALISM

We consider graphene's tight-binding Hamiltonian

$$H = -t_{i,j} \sum_{\langle i,j \rangle} (c_i^\dagger c_j + \text{H.c.}), \tag{1}$$

where c_i ($c_i^\dagger$) annihilates (creates) an electron at site i and $\langle i,j \rangle$ stands for pairs of nearest-neighbor atoms. We use the value of $t_{i,j} = 2.7$ eV for the in-plane nearest-neighbor hopping parameter and, when modeling the region of bilayer graphene, we use $t_{ij,\perp} = 0.381$ eV for the interlayer coupling [34]. The extended linear defects are constructed by rearranging the positions of the atoms in the defect region. As shown in Fig. 1, this modifies the topology of the lattice and thus changes pristine graphene's Hamiltonian in Eq. (1). For the grain boundaries defined by the 585 and 5757 linear defects (studied in Secs. III and IV), we followed several reported results [35–38] by modifying the topology of the lattice at the defect while considering the hopping parameter values unaffected in comparison to defect-free graphene (observe that the coordination number is kept constant for the atoms at these defects and the atomic separations ranging 1.38–1.44 Å [6,39] imply variations smaller than 5% in the hopping terms).

Coherent transport across grain boundaries in graphene is studied within the Landauer-Büttiker formalism, which relates the conductance $G(E)$ at a given energy E to the transmission function $T(E)$ between the contacts as

$$G(E) = G_0 T(E), \tag{2}$$

with $G_0 = 2\frac{e^2}{h} \approx \frac{1}{12.5k\Omega}$. In the context of the previously referred first approach to scattering problems by GBs, the transmittance $T(E)$ is evaluated by means of the recursive Green's-function approach using a two-terminal device configuration with contacts represented by the semi-infinite ideal graphene leads

$$T = Tr[\Gamma_L G_S^\dagger \Gamma_R G_S], \tag{3}$$

where G_S is the retarded Green's function of the system, given by [40]

$$G_S = [E'I - H_S - \Sigma_L - \Sigma_R]^{-1}. \tag{4}$$

In these expressions H_S is the Hamiltonian for the scattering region, $\Sigma_{L(R)} = t^2 g_{L(R)}$ stand for the self-energies coupling the scattering region to the leads, while E' is a shorthand for $E' = E + i\eta$, with $\eta \to 0$. The self-energies and the broadening function $\Gamma_{L(R)} = i(\Sigma_{L(R)} - \Sigma_{L(R)}^\dagger)$ [40] are calculated

from the electrode's Green's function $g_{L(R)}$ also obtained numerically using a recursive technique [41].

Charge and current are intimately related through the continuity equation. The connection with the Green's function arises from the quantum statistical average of the bond charge current operator, $\hat{J}_{ij} = \frac{e}{i\hbar}[t_{ji}c_j^\dagger c_i - t_{ij}c_i^\dagger c_j]$, which is related to the lesser Green's function $G^<_{ji}(E)$ [40,42]. In a steady state the bond charge current including spin degeneracy is

$$J_{ij} = I_0 \int_{E_F^-}^{E_F^+} dE[t_{ji}G^<_{ij}(E) - t_{ij}G^<_{ji}(E)], \tag{5}$$

where $E_F^\pm = E_F \pm eV/2$, while I_0 stands for the natural unit of bond charge current density being given by $I_0 = 2e/h \approx 77.5\ \mu$A/eV.

The lesser Green's function in the absence of interactions can be solved exactly giving $G^<(E) = G_S(E)[\Gamma_L f_L + \Gamma_R f_R]G_S^\dagger(E)$, where $f_{L(R)}$ is the Fermi distribution of the left (right) contact and t_{ji} is the hopping parameter between sites j and i. The bond current J_{ij} can be visualized as a bundle of flow lines bunched together along a link joining the two sites.

Complementary to the current density, the charge density at site j can also be expressed using the lesser Green's function as

$$\rho_{(j)} = \frac{e}{2\pi i}\int_{E_F-eV/2}^{E_F+eV/2} dE G^<_{j,j}(E). \tag{6}$$

It is noteworthy that at low bias and low temperature the charge density ρ, has the same distribution of the local density of states (LDOS). Given that we are interested in how charge and current distributions are related, to keep explanations and figures as simple as possible, we will refer from now on to the LDOS as charge distribution, with no loss of generality.

In addition to the Landauer-Buttiker formalism [see Eq. (2)], it has been shown [18,19] how can we compute the low-energy limit of the conductance across this kind of defect lines. Interestingly, at low temperatures, the conductance across a defect line of size W [see Fig. 2(a)] turned out to be linear in $K_F W$ and proportional to the transmittance [see Eq. (3)] close to the Dirac point ($E \to 0$):

$$G(E) = W\frac{g_v g_s}{4\pi}\left|\frac{E}{\hbar v_F}\right| G_0 T(E). \tag{7}$$

The gate voltage V_g is nothing more than the spatial potential distribution created by the substrate's charge distribution. We have estimated V_g for the GBs from the capacitor law

$$V_g = \frac{qnd}{\epsilon A}, \tag{8}$$

where n stands for the carrier density, d is the thickness, and ϵ is the dielectric constant of the substrate. In order to convert the experimentally measured gate voltage into carrier density n we use the relation $V_g = n/\alpha$, where $\alpha = 2.5 \times 10^{12}\ \mathrm{m^{-2}\,V^{-1}}$ is a geometry-related factor. From here onward, we will only consider the carrier density to be $n = g_s g_v K_F^2/4\pi$, where K_F is the momentum at the Fermi energy and g_v (g_s) stands for the valley (spin) degeneracy. Finally, as in graphene E_F and

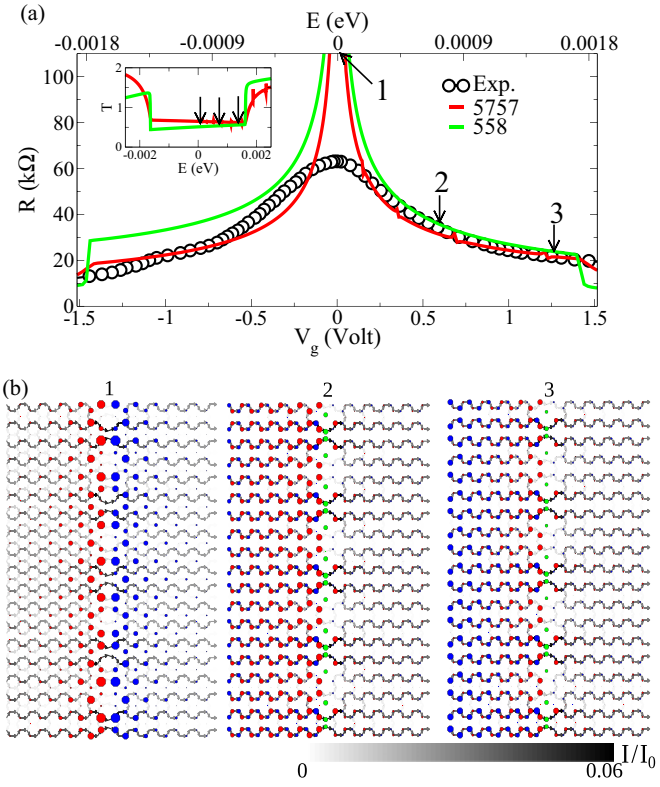

FIG. 2. (Color online) (a) Resistivity across the grain-boundary structures 5757 and 585, compared to the experimental results of Tsen *et al.* [12]. Inset: Transmission function. Here we used an armchair ribbon with $g_s = 2$, $g_v = 1$, $N = 56$ atoms along the width and making further correspondence to $W = 1\ \mu$m. (b) Spatial distribution of charge densities and current densities over the GB for different energies: $E = 10^{-7}$ eV, $E = 7 \times 10^{-4}$ eV, and $E = 14 \times 10^{-4}$ eV. The charge densities are schematically represented here for a narrower ribbon. The current densities are evaluated at different sites. The color of the arrow represents the magnitude of the electric current between any two neighboring sites, which are linearly normalized to the maximum value.

K_F are proportional at low energy, $E_F = \hbar v_F K_F$, then

$$V_g(E) = \frac{1}{\alpha}\frac{g_s g_v}{4\pi}\left(\frac{E}{\hbar v_F}\right)^2. \tag{9}$$

From Eqs. (7) and (9) one can expect that the resistance of a periodic defect line, at low temperatures and in the linear regime, should behave as

$$R = \frac{1}{G} \propto \frac{1}{\sqrt{V_g}}. \tag{10}$$

This square-root dependence on V_g should be clear from the experimental measurements of the resistivity across a grain boundary.

III. MODIFIED CONDUCTANCE QUANTIZATION IN THE PRESENCE OF THE LINEAR DEFECT

The study of scattering by extended defects is becoming increasingly more relevant, specially after the recent work by Tsen *et al.* [12], where the authors made electric measurements

across a single grain boundary. They have found that the transport properties of these systems are strongly dependent on the GB's microscopic details.

Using Eqs. (7) and (10) we calculate the resistance across two linear defects, the 5757 and the 585, and compare them with the experimental result from Tsen *et al.* (black circles)—Fig. 2(a). We verify that they agree to a good extent for V_g not too close to the Dirac point. The disagreement (at low carrier densities) between the experiment and our prediction is due to the effect of puddles [43–45] originating from disorder induced charge-carrier density fluctuations along the graphene flake. Electrons moving in such a fluctuating Fermi-level landscape will effectively propagate with an averaged conductance. This has enormous consequences when the sample's average Fermi level is brought close to the Dirac point since there the physics is completely dominated by the charge-carrier density fluctuations. Such drastic fluctuations around a nearly zero Fermi level effectively prevent electrons from *seeing* a local Fermi level that sits close enough to the Dirac point, and thus they do not feel the high resistance associated with very low charge-carrier densities [46]. The results presented in Fig. 2(a) were obtained by considering an armchair ribbon with $N = 8132$ sites ($g_s = 2$, $g_v = 1$, and $W \approx 1\ \mu$ m). The electronic properties at low-energy regimes are obtained by a rescaling of the electronic properties of an armchair ribbon with $N = 500$ sites.

The transport properties of these different linear defects are qualitatively similar. In the inset of Fig. 2(a) we show the electronic transmission and how it depends on the detailed geometry of the GB. In the continuum low-energy limit, both the 585 and the 5757 defects have a metallic behavior with a flat band crossing the Fermi level.

The spatial distribution of charge density (for different energies) of a 585 linear defect is shown in Fig. 2(b). The density on each atomic site is represented as a disk. The different colors (red and blue) identify the sublattice, while the magnitude of the disk's radius is proportional to the charge density at that site. We can see that the closer we are to the Dirac point ($E = 10^{-7}$ eV) the more localized the charge is in the region of the GB. We also plot in Fig. 2(b) the distribution of charge density for higher energies. In this case, a higher dispersion of the charge is apparent mainly before the 585 structure: the line defect acts as a potential wall.

The corresponding current densities are also shown in Fig. 2(b), being evaluated at different sites using Eq. (5). The color of the arrow represents the magnitude of the electric current between any two neighboring sites, which are linearly normalized to the maximum value, according to the greyscale bar. For all the plotted energies, we observe that before and after the linear defect, the current flows in a specific horizontal pattern along armchair paths (streamlines) skipping some horizontal bonds, in accordance with recent *ab initio* calculations of the current densities in pristine armchair graphene ribbons [47]. Here, with the linear defect, it is interesting to observe how the current gives priority to some paths within the defect line, also in a periodic pattern. One can also see that the current density is smaller for the first represented energy (i.e., $E = 10^{-7}$ eV), as would be expected due to the localized nature of the charge density around the defect for this energy.

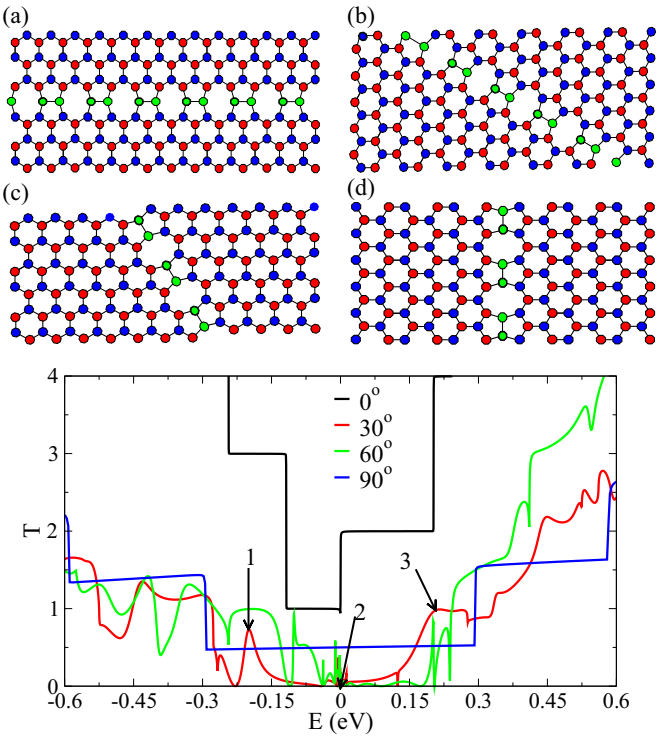

FIG. 3. (Color online) Schematic representation of a linear defect 585 at different orientation angles (a) 0°, (b) 30°, (c) 60°, and (d) 90°. (e) Transmission probability for each angle. The ribbon has $N = 56$ sites in the width.

IV. LINEAR DEFECT ORIENTATION

The transmission across linear defects is known to significantly depend on their orientation angle [19,48,49]. In Figs. 3(a)–3(d), we show schematic representations of four different orientations of a 585 extended defect in a graphene ribbon: $\theta = 0°$, 30°, 60°, and 90°. In Fig. 3(e) we plot the transmission probability as a function of the energy for these different angles of incidence at the defect. For all cases, we see that the particle-hole symmetry is broken due to the translation symmetry breaking introduced by the defect.

For $\theta = 0°$, as already studied in Refs. [6] and [36], the presence of the defect line located in the middle of the ribbon does not alter the metallic character observed in the transmission spectrum of a pristine armchair ribbon of the same width, furthermore it provides an additional channel due to the metallic nature of the defect.

Figure 3(e) also shows that for $\theta = 30°$ and 60° there are regions of vanishing transmission (opening of transport gap) close to the Dirac point. To further investigate the origins of these oscillations in the transmission, in Fig. 4 we map the charge and current density distributions for the selected energies indicated (by the arrows 1, 2, and 3) in Fig. 3(e).

The first energy (arrow 1) corresponds to a transmission resonance at an energy $E = -0.21$ eV, which is typical of resonant tunneling structures, where the continuum background is strongly suppressed at the discrete state localization. The associated charge and current density distribution are shown in Fig. 4(a). A high current density exactly following the defect line reveals its metallic character. Close to the contacts and

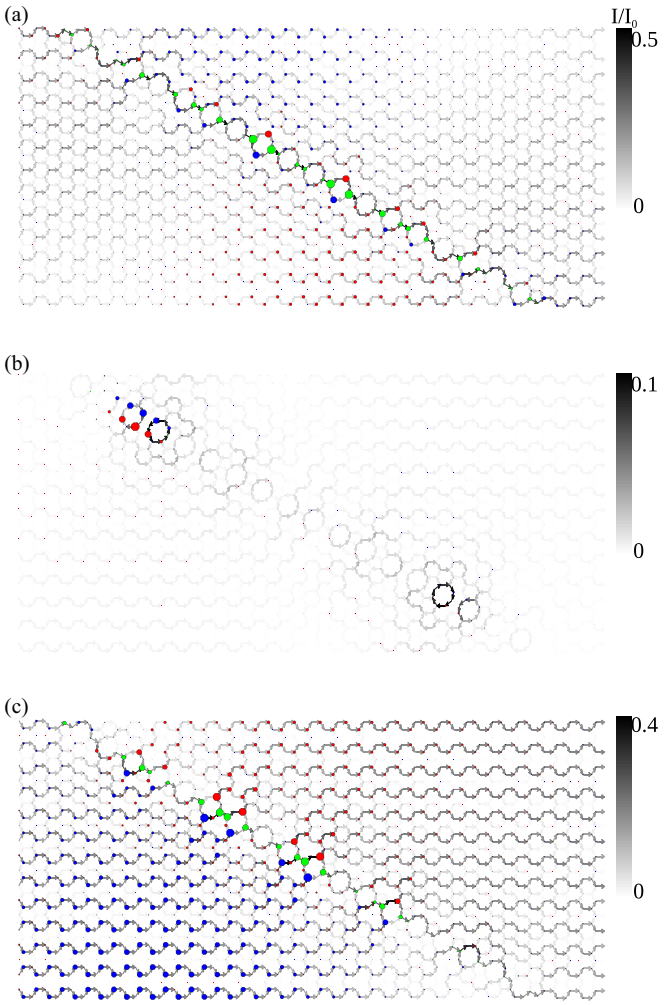

FIG. 4. (Color online) Spatial distribution of charge densities and current densities over the linear defect 585 with a orientation angle of $\theta = 30^\circ$, corresponding to the energies indicated by the numbered arrows in Fig. 3(b): $E = -0.21$ eV, $E = 1 \times 10^{-7}$ eV, and $E = 0.21$ eV.

far from the defect line, the current flow splits again into streamlines [47]. A similar behavior (high current density located along the linear defect) is found for resonances at angle of 60° (not shown here). We also found that the resonances of the first channel in the angles 30° and 60° are robust structures independent from W. The present results suggest an image of Fano-type resonances, a finite coupling between the localized state associated to the linear defect and the delocalized continuum states associated with the armchair ribbon.

In Fig. 4(b), we show the charge and current density distribution for the second selected energy [arrow 2 in Fig. 3(e)], corresponding to a vanishing transmission close to the Dirac point. Interference in charge and current density on both sides of the linear defect can be seen, as well as on the linear defect. For this low energy we observe that the charge distribution is highly localized in part of the defect. The current seems not to flow, with its maximum local values circulating around the octagons where the charge is concentrated and around octagons symmetrically positioned with respect to the middle of the linear defect. Note that the directions of the small arrows representing the local current flow around the octagons is different for Fig. 4(b) (local loopings) and Fig. 4(a) (net flow). The backscattering is evident. Therefore we conclude that at low energies, i.e., close to the Dirac point, the suppression of the transmission, at the first electronlike plateau, is due to charge localization and backscattering of a defect-related mode of the 585 defect line.

Figure 4(c) corresponds to an energy value of $E = 0.21$ eV. One can see that the current throughout the ribbon is not uniform and forms ambiguous paths. At this energy, the current-density amplitude also flows across the defect, being greater in the edge region than in the center of the ribbon. The flow is mostly perpendicular to the linear defect. Note that an electron can travel between the source and the drain via many different transport channels. The local electric current profile at a given energy is nothing more than the result from the interference between all the active transport channels at that energy. In particular, the existence of current loops for some defect orientations (see the panels of Fig. 4), simply results from particular interference patterns arising from the different blockade of distinct transport channels by the linear defect. Moreover, the particular local current patterns that are observed result from the interplay between the different components of the nanostructure: linear defect topology and orientation, edge type, and width of the graphene ribbon. In Fig. 3(b), for $\theta = 90^\circ$, the first plateau does not present interference oscillations; the transmission is reduced in the vicinity of the Dirac point, due to the coupling of extended states at the edges with localized ones at the defect line. The oscillations at the high-energy range are simply Fabry-Perot interference effects.

V. BILAYER GRAPHENE AS A GRAIN BOUNDARY

In this section we investigate the electronic transport properties of a grain boundary defined by an overlap between two semi-infinite monolayer graphene regions, forming a bilayer region as represented in Fig. 5(a). Such overlaps have been experimentally observed [12]. Here, to focus on the effects of the bilayer region on the transmission, we consider periodical boundary conditions, avoiding edge localization effects.

Figures 5(b) and 5(c) show the transmission $T(E)$ as a function of energy across a bilayer region of length L corresponding to 80 and 320 atoms superposed, respectively. We consider both the AB (Bernal) and AA stacking cases for the overlap regions. For both of them oscillations in the transmission are observed, with their frequency increasing for increasing overlap length L, in agreement with previous calculations for similar overlaps [31]. This can be qualitatively understood by remembering that in such systems, the transmittance is set by the wave-function matching at the monolayer-bilayer interfaces. A monolayer eigenstate incoming from the left is going to be partially transmitted into the bilayer region and partially reflected back into the left monolayer. The portion of the wave-function transmitted into the bilayer region is going to propagate (acquiring a complex phase) until the second interface (bilayer-monolayer) and there it will undergo a similar scattering process: it is going to be partially reflected

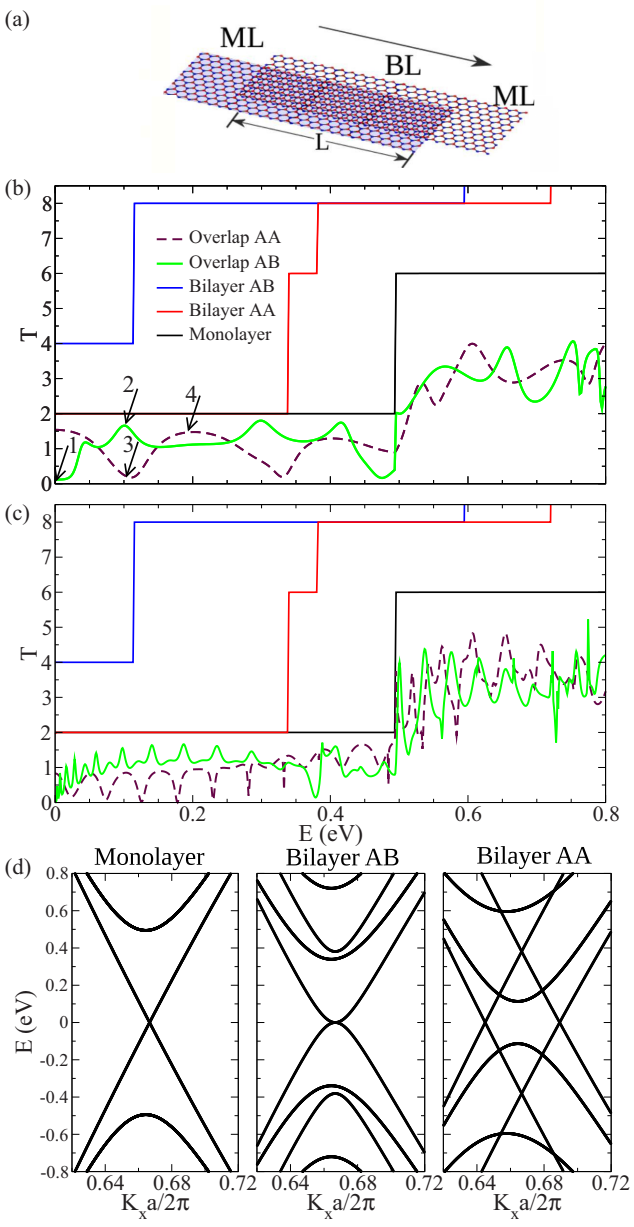

FIG. 5. (Color online) (a) Schematic representation of the overlap between two graphene monolayers, forming a bilayer region of length L. (b) Transmission throughout a bilayer region of length L corresponding to 80 atoms superposed. Both AA and AB stackings are considered for the overlap (bilayer region). For comparison is shown the transmission through a pristine monolayer and pristine bilayers AA and AB of same width. (c) Same as in (b), showing now the transmission throughout a bilayer region of length L corresponding to 320 atoms superposed. (d) Band structures for pristine monolayer and pristine bilayers AA and AB of same width.

back to the bilayer and partially transmitted into the right monolayer. The resultant standing wave, in particular, the weight associated with each of its components (channels), is going to be the direct result of this interference process and will thus strongly depend on the length of the bilayer region and on the wave number associated with each of those channels. The phases acquired by each of the wave function's components of the bilayer region at the second interface are going to be smaller for shorter bilayer regions (i.e., shorter L). In such cases, oscillations in the transmittance will require a greater change of the eigenstates' wave number, i.e., a greater increase in energy, as observed in both panels of Fig. 5. For comparison, we also show in Figs. 5(b) and 5(c) the transmission through a pristine monolayer and pristine bilayers AA and AB (considering the same width, 40 atoms, to which periodic boundary conditions are applied). One can see that the transmission through the pristine monolayer and bilayers is always higher than the transmission throughout the overlapped region. This is due to the presence of the interfaces, that act as scattering centers decreasing the system's transmission. Figure 5(d) shows the band structure for pristine monolayer and pristine bilayers AA and AB (of the same width and also with periodical boundary conditions), which helps in understanding the origin of the plateaus in the transmission for each case. At low energies, in the case of AB stacking there is only one conducting channel, whereas in AA stacking there are always two conducting channels for each valley. This partially explains why in general the low-energy transmission for the AB bilayer structure is smaller than that for the AA bilayer structure. But in addition to this, we can easily check that the boundary condition at a monolayer-bilayer AA interface can be completely satisfied at low energies without the need for reflected components in the monolayer region. The same does not happen for the case of the monolayer-bilayer AB interface. Therefore, the upper bound for the transmission at low energies is smaller in the bilayer AB case than in the bilayer AA case. Nevertheless, and by appropriately choosing the bilayer region length L, we can still make bilayer AB case's low-energy transmission higher than that of the bilayer AA case.

In Fig. 6 we map the spatial distribution of charge density and local current density on each of the overlapping (AB stacking) graphene monolayer ribbons. Figures 6(a) and 6(b) show such maps corresponding to the energies $E = 0.001$ eV and $E = 0.1$ eV, indicated by arrows 1 and 2 in Fig. 5, respectively a minimum and a maximum value of transmission in the low-energy limit. For $E = 0.001$ eV, i.e., in Fig. 6(a), the charge density is localized mainly on the left semi-infinite monolayer, which corresponds to the bottom layer in the bilayer region. On the right semi-infinite monolayer (i.e., the top layer of the bilayer region), the charge density rapidly decreases from the left to the right. In particular, its charge density is insignificant in the monolayer region. In the regions with nonvanishing charge density of each layer, the charge density typically concentrates on only one sublattice: the nondimer sublattice. This effect comes from the sublattice asymmetry introduced by the AB stacking in bilayer graphene [50,51]. Moreover, for this energy, the current density is very low on both layers. On the other hand, for $E = 0.1$ eV (which corresponds to a peak in the transmission), we can see in Fig. 6(b) that again the charge seems to be polarized on the nondimer sublattice in the central part of the bilayer region. However, a careful observation of other parts of the bilayer region shows that the charge is more homogeneously distributed over both sublattices there, thus allowing electron hopping between sites and between layers [52,53], as observed in the pattern of the zigzag current density streamlines.

Similarly, in Fig. 7 we show the charge and current density distribution for the case of the two monolayers with

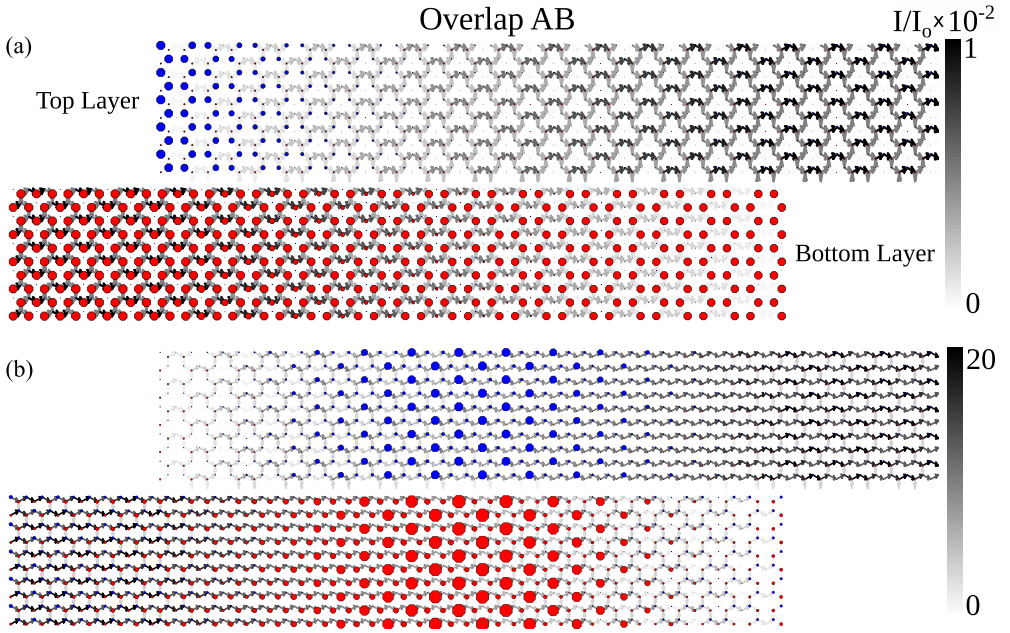

FIG. 6. (Color online) Charge and current density distributions for the nanostructure composed of two graphene (monolayer) ribbons that partially overlapped (AB stacked in the overlap/bilayer region). The two panels stand for two different energies: (a) $E = 0.001$ eV, which corresponds to a minimum of transmission (indicated by arrow 1 in Fig. 5). (b) $E = 0.1$ eV, which corresponds to a maximum of transmission (indicated by arrow 2 in Fig. 5).

an AA-stacking overlap region. Figure 7(a) corresponds to $E = 0.11$ eV (the minimum in transmission indicated by arrow 3 in Fig. 5), while Fig. 7(b) corresponds to $E = 0.2$ eV (the resonance in transmission indicated by arrow 4 in Fig. 5). For both energies, there is a clear charge wave along the bilayer length with charge oscillating between the two layers. Similarly, the current also oscillates between layers. However, comparing charge and current densities in each layer, one can see an interesting behavior: for the energy corresponding to low transmission, Fig. 7(a) shows that there is a clear imbalance, since the electronic charge density and the current density are concentrated on different parts of the bilayer

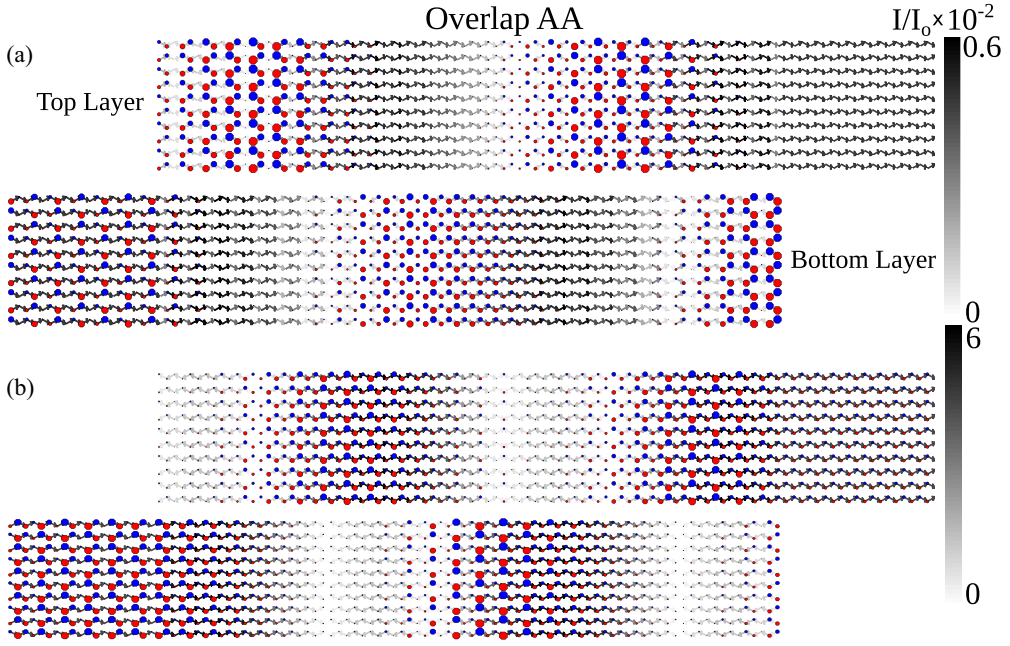

FIG. 7. (Color online) Charge and current density distributions for the nanostructure composed of two graphene (monolayer) ribbons that partially overlapped (AA stacked in the overlap/bilayer region). The two panels stand for two different energies: (a) $E = 0.11$ eV, which corresponds to a low transmission (indicated by the arrow 3 in Fig. 5). (b) $E = 0.2$ eV, which corresponds to a maximum of transmission (indicated by the arrow 4 in Fig. 5).

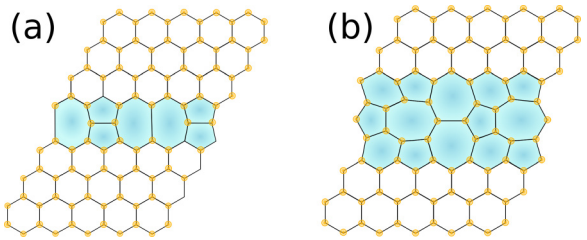

FIG. 8. (Color online) Scheme of two grain boundaries proposed in the context of *ab initio* works both on graphene and on boron nitride. (a) The 7557 defect line [33] and (b) the $t7t5$ defect line [32]. In these schemes we highlight in blue the region of the grain boundary.

region. On the other hand, in Fig. 7(b), i.e., for the energy corresponding to high transmission, we again observe a charge and current oscillation between layers along the length of the bilayer region, but now these are in phase, with the maximum current density spatially coinciding with the maximum charge density. Also note the higher current densities associated with the later energy (see the different current greyscale bar).

VI. TRANSPORT ACROSS THREE PERIODIC GRAIN BOUNDARIES: TRANSFER-MATRIX APPROACH

In this section we use the transfer-matrix formalism [18] to study the electronic transport across extended grain boundaries in the scope of the single-particle first-neighbor tight-binding model of (infinite) monolayer graphene. This method is entirely equivalent to the recursive Green's-function numerical method used up to this point of the paper. It reduces the electronic scattering problem to a set of matrix manipulations easy to work out by any computational algebraic calculator, and thus gives rise to an analytic solution of the problem.

We will concentrate on a particular class of zigzag aligned periodic GBs that separates grains with the same orientation (also known as zero misorientation angle GBs) and has a periodicity that allows for intervalley scattering of low-energy electrons. When the periodicity of the zigzag aligned GBs is a multiple of 3, both Dirac points (as well as the Γ point) are mapped into $k_x a = 0$—see Figs. 9(c) and 9(d). Therefore, and in contrast with what happens for the pentagon only 585 and 5757 GBs [16,18,19,27,28], linear momentum conservation does not forbid low-energy electrons from scattering between valleys. Nevertheless, and if we want to know how much intervalley scattering is a particular GB going to generate, we need to explicitly compute the boundary condition matrix originating from its tight-binding microscopic model.

From the diversity of GBs belonging to this class, we have chosen to investigate some that have been recently suggested in the context of *ab initio* works both on graphene and on boron nitride: the 7557 grain boundary [33] and the grain boundary [32] (see Fig. 8). As we will see ahead, these GBs controllably scatter electrons from one valley to the other and can thus be regarded as a useful nanostructure for valleytronics circuits, whenever the desire is to destroy valley polarization.

A periodic GB preserves the crystal's translation invariance along the GB direction. Therefore, by Fourier transforming the system's tight-binding Hamiltonian along this direction, we can cast the problem of electronic transport in a two-

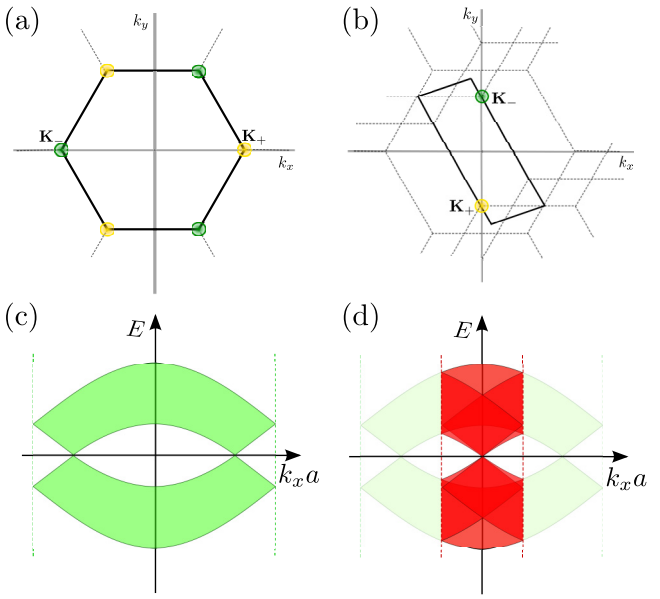

FIG. 9. (Color online) (a) FBZ of pristine graphene (whose direct lattice vectors can be chosen to be $\mathbf{u}_1 = a(1,0)$ and $\mathbf{u}_2 = a(-1,\sqrt{3})/2$). (b) FBZ of graphene whose unit cell has thrice the size of that of pristine graphene in the zigzag direction (direction of $\mathbf{u}_1$). In this case, the direct lattice vectors can be chosen to be $3\mathbf{u}_1$ and $\mathbf{u}_2$ (as done in Figs. 15 and 16). (c) Spectrum of pristine graphene projected along the k_x direction (parallel to the GB). (d) Comparison between the k_x-projected spectrum of (unfolded) pristine graphene (light green) and the same spectrum after a triple folding (red): in the latter, the two valleys (and the Γ point) are mapped into $k_x a = 0$.

dimensional (2D) crystal with a GB at its center as a problem of electronic transport on a quasi-1D crystal with a localized defect at its center.

In order to work out this problem we will proceed as in Ref. [18]. From pristine graphene's Hamiltonian we start by writing the tight-binding equations away from the grain boundary (see Figs. 15 and 16 for notation clarification)

$$-\frac{\epsilon}{t}\mathbf{A}(n) = W_A^{\dagger}\mathbf{B}(n-1) + \mathbf{B}(n), \tag{11a}$$

$$-\frac{\epsilon}{t}\mathbf{B}(n) = \mathbf{A}(n) + W_A\mathbf{A}(n+1), \tag{11b}$$

where we have used the notation $\mathbf{Z}(n) = [Z_1(n), Z_2(n), Z_3(n)]^T$ for $Z = A, B$ (sublattice identifier). Note that the notation is hiding the dependency of the A_i and B_i on k_x, the momentum along the grain-boundary direction. In the above expressions, ϵ and t stand respectively for the energy and pristine graphene's hopping parameter, while n gives the number of direct lattice vector $\mathbf{u}_2 = (-1,\sqrt{3})a/2$ translations away from the defect (see Figs. 15 and 16). The matrix W_A reads

$$W_A = \begin{bmatrix} 1 & 1 & 0 \\ 0 & 1 & 1 \\ e^{3ik_x a} & 0 & 1 \end{bmatrix}. \tag{12}$$

We can write the above tight-binding equations in the form

$$\begin{bmatrix}\mathbf{B}(n)\\ \mathbf{A}(n)\end{bmatrix} = \mathbb{Q}_1 \begin{bmatrix}\mathbf{A}(n)\\ \mathbf{B}(n-1)\end{bmatrix}, \tag{13a}$$

$$\begin{bmatrix}\mathbf{A}(n)\\ \mathbf{B}(n-1)\end{bmatrix} = \mathbb{Q}_2 \begin{bmatrix}\mathbf{B}(n-1)\\ \mathbf{A}(n-1)\end{bmatrix}, \tag{13b}$$

where the matrices $\mathbb{Q}_1$ and $\mathbb{Q}_2$ read

$$\mathbb{Q}_1 = -\begin{bmatrix}\frac{\epsilon}{t}\mathbb{I}_3 & W_A^\dagger\\ -\mathbb{I}_3 & 0\end{bmatrix}, \tag{14a}$$

$$\mathbb{Q}_2 = -\begin{bmatrix}\frac{\epsilon}{t}(W_A)^{-1} & (W_A)^{-1}\\ -\mathbb{I}_3 & 0\end{bmatrix}, \tag{14b}$$

with $\mathbb{I}_3$ standing for the 3×3 unit matrix.

Equation (13) can be written in the form of a transfer matrix equation [18,19] relating amplitudes at the atoms of the unit cell located at $(n-1)\mathbf{u}_2$ with the amplitudes at the atoms of the unit cell located at $n\mathbf{u}_2$. Such an equation reads

$$\mathbf{L}(n) = \mathbb{T}(\epsilon,k_x)\mathbf{L}(n-1), \tag{15}$$

with $\mathbf{L}(n) = [A_1(n),B_1(n),A_2(n),B_2(n),A_3(n),B_3(n)]^T$, and the transfer matrix, $\mathbb{T}(\epsilon,k_x)$, given by

$$\mathbb{T}(\epsilon,k_x) = R.\mathbb{Q}_1.\mathbb{Q}_2.R^T. \tag{16}$$

In the above equation, matrix R is simply used to change from the basis $\{B_1,B_2,B_3,A_1,A_2,A_3\}$ to the basis $\{A_1,B_1,A_2,B_2,A_3,B_3\}$. It is written in Eq. (A1).

Following the method used for the cases of the 585 and 5757 defect lines [18,19], we can find a basis where the transfer matrix becomes block diagonal with three 2×2 matrices on its diagonal. In this basis the three modes of the problem are uncoupled. Moreover, around $k_x = 0$ two of these modes are low-energy (corresponding to each of the two Dirac cones), while the other is a high-energy mode.

We can understand this fact from Fig. 9(b) where one represents the first Brillouin zone (FBZ) originating from a honeycomb lattice whose direct vectors are chosen to be $3\mathbf{u}_1$ and $\mathbf{u}_2$. In such a FBZ, the two Dirac points are located at the same value of k_x, i.e., at $k_x = 0$. It is thus natural that when setting $k_x = 0$ in the transfer matrix given by Eq. (16), one obtains a transfer matrix that describes simultaneously low-energy electrons at each of the two valleys (together with an additional high-energy mode associated with the Γ-point region of the spectrum of pristine graphene).

The symbol $\Lambda(k_x)$ stands for the matrix mediating the change to the basis uncoupling the modes of the transfer matrix

$$\widetilde{\mathbf{L}}(n) = \Lambda(k_x)\mathbf{L}(n). \tag{17}$$

We will denote the states in this new basis as

$$\widetilde{\mathbf{L}} = [A_h,B_h,A_{l-},B_{l-},A_{l+},B_{l+}], \tag{18}$$

with h identifying the mode with high-energy when $k_x \approx 0$, while $l+$ and $l-$ stand for the two modes with low energy when $k_x \approx 0$, one associated with the $\mathbf{K}_-$ valley and the other with the $\mathbf{K}_+$ valley. The matrix $\Lambda(k_x)$ is explicitly written in Eq. (A2).

As previously stated, in this basis the transfer matrix, $\widetilde{\mathbb{T}}(\epsilon,k_x)$, is block diagonal and reads

$$\widetilde{\mathbb{T}}(\epsilon,k_x) = \begin{bmatrix}\mathbb{T}_h(\epsilon,k_x) & 0 & 0\\ 0 & \mathbb{T}_{l-}(\epsilon,k_x) & 0\\ 0 & 0 & \mathbb{T}_{l+}(\epsilon,k_x)\end{bmatrix}, \tag{19}$$

where the three transfer matrices associated with each of the uncoupled modes are written in Eqs. (A3).

A. Transmittance across the 7557 and the $t7t5$ grain boundaries

In a similar manner, the tight-binding Hamiltonian describing the electronic structure close to the grain boundary can be used to write the tight-binding equations for the defect. With these we can compute a boundary condition relating amplitudes on either side of the defect,

$$\mathbf{L}(1) = \mathbb{M}\cdot\mathbf{L}(-1), \tag{20}$$

where the boundary condition matrix $\mathbb{M}$ is a 6×6 matrix that depends both on the energy ϵ, x-momentum k_x and the electron hoppings characteristic of the grain boundary. In Appendix B we compute these matrices for the two grain boundaries we are investigating: the 7557 and the $t7t5$ grain boundaries (see Figs. 15 and 16).

Note that by expressing this boundary condition matrix in the basis that uncouples the modes of the transfer matrix $\mathbb{T}(\epsilon,k_x)$,

$$\widetilde{\mathbb{M}} = \Lambda(k_x a)\cdot\ \mathbb{M}\cdot[\Lambda(k_x a)]^{-1}, \tag{21}$$

we can conclude that in general, it mixes all three modes of the matrix $\mathbb{T}(\epsilon,k_x)$.

Given this, we now have all the ingredients needed to compute the coefficients involved in the electronic scattering by such defects. An incoming electronic wave from $n=-\infty$ will be scattered by the defect at $n=0$ producing a reflected and a transmitted component. The wave function on each side of the defect will then be given by

$$\widetilde{\mathbf{L}}(n<0) = \lambda_{i>}^{n+1}\,\mathbf{\Psi}_i^{>} + \sum_{j=1}^{r_<}\rho_{ij}\,\lambda_{j<}^{n+1}\,\mathbf{\Psi}_j^{<}, \tag{22a}$$

$$\widetilde{\mathbf{L}}(n>0) = \sum_{j=1}^{r_>}\tau_{ij}\,\lambda_{j>}^{n-1}\,\mathbf{\Psi}_j^{>}, \tag{22b}$$

where ρ_{ij} and τ_{ij} are, respectively, the reflection and transmission scattering amplitudes from an incoming (from $n=-\infty$) state, $\mathbf{\Psi}_i^{>}$, into reflected, $\mathbf{\Psi}_j^{<}$, and transmitted, $\mathbf{\Psi}_j^{>}$, outgoing states. Finally, by imposing the corresponding boundary condition [see Eqs. (20) and (21)], we can compute the coefficients ρ_{ij} and τ_{ij} for a given energy and a given longitudinal momentum.

For both the $t7t5$ and the 7557 grain boundary we have set the hopping parameters in the region of the grain boundary by estimating the corresponding carbon-carbon distances originating from the *ab initio* results of Refs. [32] and [33], and then using the parametrization [54]

$$\tau(r_{ij}) = \left(\frac{r_{ij}}{a_0}\right)^{-\alpha_2}\exp\left[-\alpha_3\times\left(r_{ij}^{\alpha_4}-a_0^{\alpha_4}\right)\right], \tag{23}$$

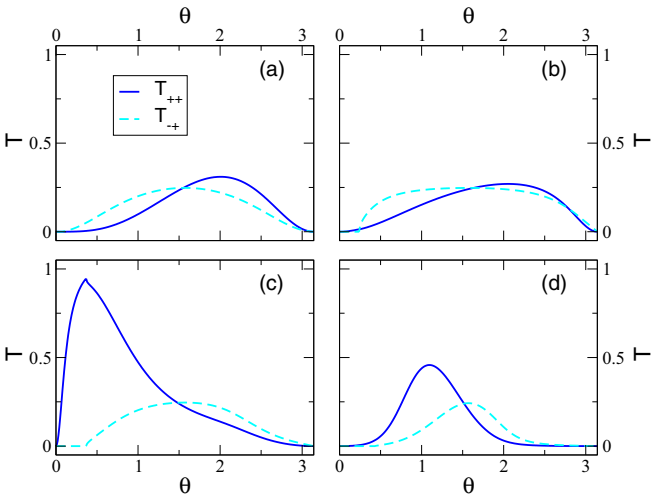

FIG. 10. (Color online) Transmittance in terms of the incidence angle (incoming electron chosen to be on the valley $\mathbf{K}_+$ Dirac point) for the 7557 grain boundary. Panels (a)–(d) correspond to scattering processes occurring at energies of, respectively, $0.01t$, $0.1t$, $0.3t$, and $0.5t$. The hopping parameters (see Fig. 15) were set at $\xi = 0.98$, $\gamma = 0.94$, and $\beta = 0.1$. The dark blue curve stands for the transmittance preserving the valley degree of freedom (electron from the $\mathbf{K}_+$ below the GB scattering scatters to the same valley above the GB, i.e. $T_{++} = |\tau_{++}|^2$). The dashed light blue curve stands for the intervalley transmittance (electron at the $\mathbf{K}_+$ valley below the GB scattering into the valley $\mathbf{K}_-$ above the GB, i.e. $T_{-+} = (v_-/v_+)\,|\tau_{-+}|^2$; $v_\pm$ stands for the velocity of the mode $l\pm$).

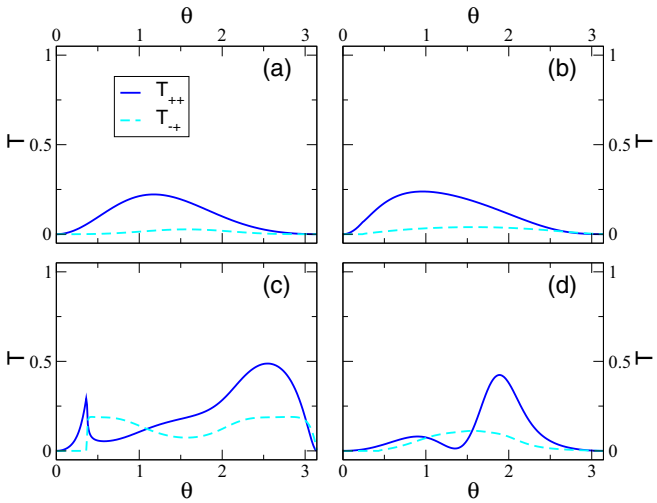

FIG. 11. (Color online) Transmittance in terms of the incidence angle (incoming electron chosen to be on the valley $\mathbf{K}_+$ Dirac point) for the $t7t5$ grain boundary. Panels (a)–(d) correspond to scattering processes occurring at energies of, respectively, $0.01t$, $0.1t$, $0.3t$, and $0.5t$. The hopping parameters (see Fig. 16) were set at $\xi_1 = 1.06$, $\xi_2 = 0.95$, $\xi_3 = 0.83$, $\xi_4 = 0.80$, $\xi_5 = 1.30$, $\xi_6 = 1.05$, $\gamma_1 = 1.23$, $\gamma_2 = 1.20$, $\gamma_3 = 1.18$, and $\gamma_1 = 1.36$. The dark blue curve stands for the transmittance preserving the valley degree of freedom (electron from the $\mathbf{K}_+$ below the GB scattering scatters to the same valley above the GB, i.e., $T_{++} = |\tau_{++}|^2$). The dashed light blue curve stands for the intervalley transmittance (electron at the $\mathbf{K}_+$ valley below the GB scattering into the valley $\mathbf{K}_-$ above the GB, i.e., $T_{-+} = (v_-/v_+)\,|\tau_{-+}|^2$; $v_\pm$ stands for the velocity of the mode $l\pm$).

where r_{ij} stands for the distance between the carbons labeled by i and j (given in units of angstroms), the adimensional parameters $\alpha_2 = 1.2785$, $\alpha_3 = 0.1383$, $\alpha_4 = 3.4490$, while a_0 is the carbon-carbon distance in pristine graphene (in units of Å).

In Fig. 10 we present the transmission probability for the 7557 grain boundary (see the scheme of Fig. 15 and Appendix B 1) of an incoming electron of the $\mathbf{K}_+$ valley. The several transmittance curves of this figure correspond to different energies and were drawn using the following hopping parameters at the defect: $\xi = 0.98$, $\gamma = 0.94$, and $\beta = 0.1$. One can see in the several panels of this figure that the intervalley scattering is comparable to the *valley-preserving* scattering. Both of them strongly depend on the energy and incidence angle, mainly due to the dependence on energy and k_x of the boundary condition matrix (see its computation in Appendix B 1).

Similar plots are presented in Fig. 11 for the $t7t5$ grain boundary (see the scheme of Fig. 16 and Appendix B 2). These were obtained with the following hopping parameters: $\xi_1 = 1.06$, $\xi_2 = 0.95$, $\xi_3 = 0.83$, $\xi_4 = 0.80$, $\xi_5 = 1.30$, $\xi_6 = 1.05$, $\gamma_1 = 1.23$, $\gamma_2 = 1.20$, $\gamma_3 = 1.18$, and $\gamma_1 = 1.36$. In general, this choice of hopping parameters gives rise to a lower intervalley scattering at low energies than what is obtained for the 7557 grain boundary.

The transmission curves in Figs. 10 and 11 (for the valley preserving scattering channel T_{++} and for the intervalley scattering channel T_{-+}) originate from the interplay between the expression of the eigenstates involved in the scattering (at a given energy) and the boundary condition matrix $\mathbb{M}$ (also energy dependent) for the grain boundary—which is determined by the microscopic details of each grain boundary (see Appendix B). The complexity of the system of equations determining the scattering coefficients ρ_{++}, ρ_{-+}, τ_{++}, and τ_{-+} [see Eqs. (20)–(22)], makes it nontrivial to unveil the physical reasons behind the different attributes of the transmission probability curves T_{++} and T_{-+} in Figs. 11 and 10. However, in the following paragraphs we discuss some of the features observed in these figures.

The attentive reader may have noticed that all the panels of Figs. 11 and 10 show a discontinuity at a critical angle $\theta_c(\epsilon)$ in the derivative of both the valley preserving transmission channel T_{++} (blue full curves) and the intervalley scattering channel T_{-+} (cyan dashed curves). This critical angle is different in each of the panels, i.e., it varies with the energy of the incident electron, but for a fixed energy it does not change from one grain boundary to the other (compare Figs. 10 and 11). These discontinuities in the derivatives of T_{++} and T_{-+} are due to the opening of a new transport channel for $\theta \geqslant \theta_c(\epsilon)$, namely the channel allowing for electrons to scatter off the grain boundary jumping from one valley to the other. This is a result of the trigonal wrapping of the Dirac cones, which prevents incident electrons (from the valley $\mathbf{K}_+$) with very small incidence angle $\theta^{(i)} \approx 0$ [else, with x momentum $k_x^+(\theta^{(i)})$] to scatter to the valley $\mathbf{K}_-$ because the latter does not have any propagating state with a x momentum such that it can match that of the incident state, i.e., there is no $k_x^-(\theta)$ satisfying $k_x^-(\theta) = k_x^+(\theta^{(i)})$—see Fig. 12. This critical angle is zero for incident electrons with zero energy (since the trigonal

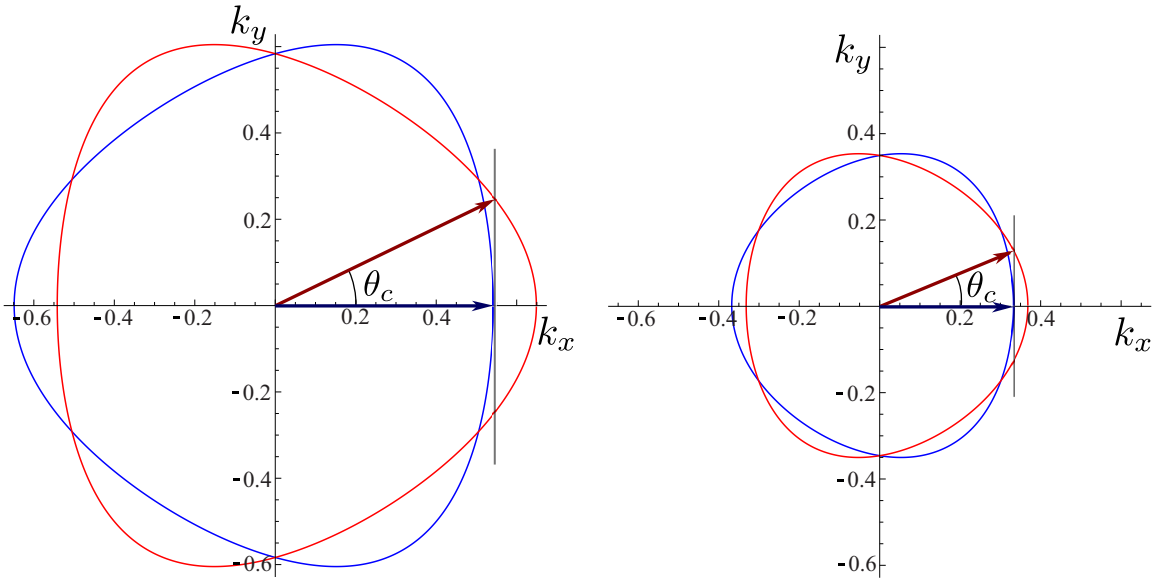

FIG. 12. (Color online) Cut of the energy spectrum around the two valleys ($\mathbf{K}_+$ in red and $\mathbf{K}_-$ in blue) at energies $0.5t$ (left) and $0.3t$ (right). The trigonal wrapping of the spectrum in each valley is clearly seen, as well as that the spectra around the two valleys are connected by $\mathbf{k} \longrightarrow -\mathbf{k}$, i.e., $E_{\mathbf{K}_\pm}(\mathbf{k}) = E_{\mathbf{K}_\mp}(-\mathbf{k})$. The critical angle θ_c for the intervalley scattering is defined by the smallest angle of incidence $\theta_c^{(i)}$ for which it is possible to satisfy linear momentum conservation along the x direction for a scattering between the valley $\mathbf{K}_+$ and the valley $\mathbf{K}_-$. That is, $k_x^+(\theta_c^{(i)}) = k_x^-(0)$, where $k_x^+(\theta_c^{(i)})$ [$k_x^-(0)$] stands for the k_x momentum in $\mathbf{K}_+$ [$\mathbf{K}_-$] valley for an angle of incidence $\theta_c^{(i)}$ (see red arrows) [transmission zero (see blue arrows)] at the energy ϵ. From the figure one can see that since the trigonal wrapping decreases with decreasing energy, then the critical angle decreases for lower energy.

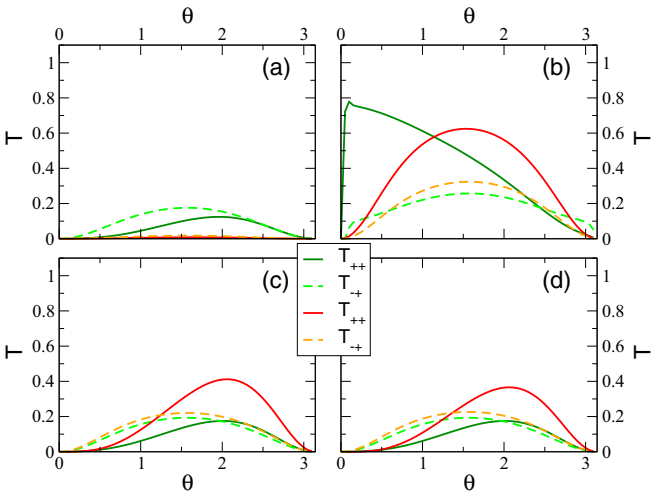

FIG. 13. (Color online) Variation of the transmission probabilities T_{++} and T_{-+} (of the 7557 grain boundary) upon modifications of the original hoppings at the grain boundary ($\xi = 0.98$, $\gamma = 0.94$, and $\beta = 0.1$) at an energy $E = 0.01t$ [compare with Fig. 10(a)]. The green full and dashed curves in (a) stand for the T_{++} and T_{-+} of a 7557 grain boundary with all the original hoppings divided by 2, i.e., $\xi/2$, $\gamma/2$, and $\beta/2$, while the red full/orange dashed curves were obtained with all the original hoppings divided by 10, i.e., $\xi/10$, $\gamma/10$, and $\beta/10$. Panel (b) stands for T_{++} and T_{-+} with all the hoppings set to t (green curves) and to $2t$ (red/orange curves). The transmission curves shown in panel (c) were obtained by keeping all the hoppings fixed except ξ that was multiplied by 0.8 (green curves) and by 1.2 (red and orange curves). Similarly, the transmission curves shown in panel (d) were obtained by keeping all the hoppings fixed except γ, that was multiplied by 0.8 (green curves) and by 1.2 (red and orange curves).

wrapping vanishes at zero energy), increasing with energy as can be seen in Fig. 12. In particular, the peaks in T_{++} that can be seen at small incident angles in Figs. 10(c) and 11(c), are exactly due to this: the opening of the intervalley scattering channel diverts electrons from the valley preserving scattering channel, thus diminishing T_{++}.

We finalize by noting that the transmission probabilities T_{++} and T_{-+} are strongly dependent on the choice of the hopping parameters. At low energies these are the only parameters determining the boundary condition matrix and therefore controlling the system's transparency to incident electrons. Moreover, the GB's scattering profile can be strongly enhanced or suppressed by small changes of the GB's hopping parameters. Therefore, we may expect that intervalley scattering at the GB is deeply sensitive to modifications of the lattice's geometry (namely strain) in the vicinity of the GB.

In Fig. 13 (and Fig. 14) we plot the transmission probabilities T_{++} and T_{-+} for the 7557 ($t7t5$) grain boundary for incident electrons with an energy of $0.01t$, for modified hopping parameters [compare with the transmission profiles in Figs. 10(a) and 11(a)]. From these figures we can readily conclude that T_{++} and T_{-+} are strongly affected by abrupt changes of the hopping parameters. In particular, decreasing all the hoppings by the same factor (of 2 or of 10), decreases T_{++} and T_{-+} for both grain boundaries [see Figs. 13(a) and 14(a)]. These transmission probabilities become nearly zero when all the hoppings are divided by 10, which is natural to expect since by doing that we are essentially disconnecting the atoms at the grain boundary, making it more difficult for the electron wave to cross the grain boundary. When all the hoppings at the grain boundary are made equal to t, the transmission profile is strongly modified. Interestingly, the 7557 shows a valley

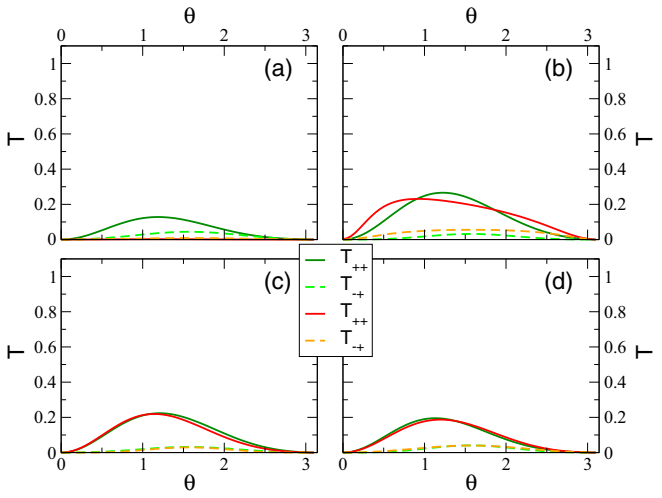

FIG. 14. (Color online) Variation of the transmission probabilities T_{++} and T_{-+} (of the $t7t5$ grain boundary) upon modifications of the original hoppings at the grain boundary ($\xi_1 = 1.06t$, $\xi_2 = 0.95t$, $\xi_3 = 0.83t$, $\xi_4 = 0.80t$, $\xi_5 = 1.30t$, $\xi_6 = 1.05t$, $\gamma_1 = 1.23t$, $\gamma_2 = 1.20t$, $\gamma_3 = 1.18t$, and $\gamma_1 = 1.36t$) at an energy $E = 0.01t$ [compare with Fig. 11(a)]. The green full and dashed curves in (a) stand for the T_{++} and T_{-+} of a $t7t5$ grain boundary with all the original hoppings divided by 2, i.e., $\xi_i/2$ and $\gamma_i/2$, while the red full/orange dashed curves were obtained with all the original hoppings divided by 10, i.e., $\xi_i/10$ and $\gamma_i/10$. Panel (b) stands for T_{++} and T_{-+} with all the hoppings set to t (green curves) and to $2t$ (red/orange curves). The transmission curves shown in (c) were obtained by keeping all the hoppings fixed except ξ_1, ξ_2, ξ_3, ξ_5, and ξ_6 that were multiplied by 0.8 (green curves) and by 1.2 (red and orange curves). Similarly, the transmission curves shown in (d) were obtained by keeping all the hoppings fixed except γ_1, γ_2, γ_3, and γ_4, that were multiplied by 0.8 (green curves) and by 1.2 (red and orange curves).

filter like T_{++} (similarly to what happens for the 558 grain boundary). Making all the hoppings at the grain boundary equal to $2t$ further modifies the transmission profiles. Finally, when we keep the smallest hopping constant while varying the other hoppings by $\pm 20\%$, the transmission probabilities do not change very much [compare Figs. 13(c) and 13(d) with Figs. 10(a), 14(c), and 14(d) with Fig. 11(a)], suggesting that the smallest hopping has an important role in controlling the transport across the grain boundaries.

VII. CONCLUSION

Let us now briefly summarize the main findings of this paper. We have shown that the electronic transport across a 5757 or 585 grain boundary oriented perpendicular to the ribbon longitudinal direction depends on the grain boundary's microscopic details, with the charge density and charge current varying from one grain boundary to the other. Nevertheless, not too close to the Dirac point (where the electron-hole puddles have a strong effect) our predictions for the resistivity of such systems (that ignore the effect of puddles) are in good accordance with experimental measurements recently done by Tsen *et al.* We have also found that the electronic transport of such systems is strongly dependent on the grain boundary's orientation. In particular, ribbons with tilted grain boundaries can have their charge transport completely suppressed at energies close to the Dirac point due to interference effects between the different transport channels (that are reflected by the grain boundary and the ribbon edges). The electronic transport along flakes with overlapping monolayers is controlled both by the stacking order and the length of the bilayer region. These determine how the different transport channels interfere to enhance or suppress the electronic transport of such systems. Finally, we have shown that the electronic transport across the $t7t5$ and 7557 three-periodic grain boundaries gives rise to intervalley scattering, which is rather sensitive to the microscopic properties of the grain boundaries.

ACKNOWLEDGMENTS

N.M.R.P. acknowledges support from EC under Graphene Flagship (Contract No. CNECT-ICT-604391) and the hospitality of the Instituto de Física of the UFRJ, where this work was completed. J.N.B.R. acknowledges Singapore National Research Foundation for its support through the Fellowship Program NRF-NRFF2012-01. C.J.P. and A.L.C.P. acknowledge São Paulo Research Foundation (FAPESP), Grant No. 2012/19060-0. Part of the numerical simulations were performed at the computational facilities from CENAPAD-SP, at Campinas State University.

APPENDIX A: BULK TIGHT-BINDING EQUATIONS

The matrix R changing from the basis $\{B_1(n), B_2(n), B_3(n), A_1(n), A_2(n), A_3(n)\}$ into the basis $\{A_1(n), B_1(n), A_2(n), B_2(n), A_3(n), B_3(n)\}$ reads

$$R = \begin{bmatrix} 0 & 0 & 0 & 1 & 0 & 0 \\ 1 & 0 & 0 & 0 & 0 & 0 \\ 0 & 0 & 0 & 0 & 1 & 0 \\ 0 & 1 & 0 & 0 & 0 & 0 \\ 0 & 0 & 0 & 0 & 0 & 1 \\ 0 & 0 & 1 & 0 & 0 & 0 \end{bmatrix}. \tag{A1}$$

The matrix mediating the basis change that uncouples the modes of the transfer matrix, $\Lambda(k_x)$, reads

$$\Lambda\left(\frac{\phi}{a}\right) = \frac{1}{\sqrt{3}} \begin{bmatrix} 1 & 0 & -\frac{e^{-i(\phi-2\pi/3)}i\sqrt{3}}{1+e^{i\pi/3}} & 0 & \frac{e^{-i2(\phi-2\pi/3)}i\sqrt{3}}{1+e^{-i\pi/3}} & 0 \\ 0 & 1 & 0 & -\frac{e^{-i(\phi-2\pi/3)}i\sqrt{3}}{1+e^{i\pi/3}} & 0 & \frac{e^{-i2(\phi-2\pi/3)}i\sqrt{3}}{1+e^{-i\pi/3}} \\ 1 & 0 & -e^{-i(\phi-\pi/3)} & 0 & -e^{-i(2\phi+\pi/3)} & 0 \\ 0 & 1 & 0 & -e^{-i(\phi-\pi/3)} & 0 & -e^{-i(2\phi+\pi/3)} \\ 1 & 0 & -e^{-i(\phi+\pi/3)} & 0 & -e^{-i(2\phi-\pi/3)} & 0 \\ 0 & 1 & 0 & -e^{-i(\phi+\pi/3)} & 0 & -e^{-i(2\phi-\pi/3)} \end{bmatrix}, \tag{A2}$$

where $\phi = k_x a$.

As just said, in this basis the transfer matrix, Eq. (16), becomes block diagonal with three 2×2 matrices in its diagonal. The three pairs of modes, h, $l+$, and $l-$, decouple and propagate independently. If we put ourselves around the Dirac point $\mathbf{K}_+ = (0,-1)\nu 4\pi/(3\sqrt{3}a)$, the upper matrix corresponds to the high-energy mode, the middle one corresponds to the Dirac cone identified by $\nu=-1$, while the lower matrix stands for the cone identified by $\nu=+1$. For a general energy and momentum these three matrices read

$$\mathbb{T}_h(\epsilon,\phi) = \frac{1}{1+e^{i\phi}}\begin{bmatrix} -1 & -\epsilon \\ \epsilon & \epsilon^2-2-2\cos\phi \end{bmatrix}, \quad \text{(A3a)}$$

$$\mathbb{T}_{l-}(\epsilon,\phi) = f(\phi)\begin{bmatrix} -1 & -\epsilon \\ \epsilon & \epsilon^2+\frac{e^{-i(\phi-\frac{\pi}{3})}-1}{f(\phi)} \end{bmatrix}, \quad \text{(A3b)}$$

$$\mathbb{T}_{l+}(\epsilon,\phi) = g(\phi)\begin{bmatrix} -1 & -\epsilon \\ \epsilon & \epsilon^2+\frac{e^{-i(\phi+\frac{\pi}{3})}-1}{g(\phi)} \end{bmatrix}, \quad \text{(A3c)}$$

where we have again used $\phi = k_x a$ and have defined $f(\phi)$ and $g(\phi)$ as

$$f(\phi) = \frac{e^{i\pi/3}-e^{-i\phi}}{1-2\cos\phi}, \quad \text{(A4a)}$$

$$g(\phi) = \frac{e^{-i\pi/3}-e^{-i\phi}}{1-2\cos\phi}. \quad \text{(A4b)}$$

APPENDIX B: BOUNDARY CONDITION OF THE 7557 AND $t7t5$ GRAIN BOUNDARIES

In this appendix we will briefly compute the boundary condition matrix associated with the two grain boundaries investigated in Sec. VI.

1. Boundary condition of the 7557 grain boundary

Let us start by computing the boundary condition matrix relating the wave-function amplitudes on either side of the 7557 grain boundary (see Fig. 15 for a scheme of its crystalline structure).

The tight-binding equations at the defect region read

$$-\frac{\epsilon}{t}\mathbf{B}(0) = \mathbf{A}(1) + \mathcal{X}^T\mathbf{D} + \mathcal{B}\mathbf{A}(0), \quad \text{(B1a)}$$

$$-\frac{\epsilon}{t}\mathbf{D} = \mathcal{X}\big(\mathbf{A}(0)+\mathbf{B}(0)\big) + \mathcal{G}\mathbf{D}, \quad \text{(B1b)}$$

$$-\frac{\epsilon}{t}\mathbf{A}(0) = \mathcal{X}^T\mathbf{D} + W_A^\dagger\mathbf{B}(-1) + \mathcal{B}\mathbf{B}(0), \quad \text{(B1c)}$$

where we use the notation $\mathbf{Z}(n) = [Z_1(n), Z_2(n), Z_3(n)]^T$ with $Z = A, B, D$. The matrices $\mathcal{X}$, $\mathcal{B}$, and $\mathcal{G}$ read

$$\mathcal{X} = \begin{bmatrix} \xi & 0 & 0 \\ 0 & 0 & \xi \\ 0 & 0 & 0 \end{bmatrix}, \quad \text{(B2a)}$$

$$\mathcal{B} = \begin{bmatrix} 0 & 0 & 0 \\ 0 & \beta & 0 \\ 0 & 0 & 0 \end{bmatrix}, \quad \text{(B2b)}$$

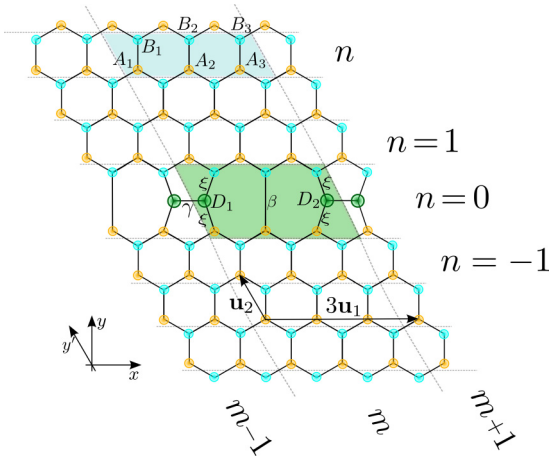

FIG. 15. (Color online) Crystalline structure of the 7557 grain boundary [33]. The region of the defect line is highlighted in blue.

$$\mathcal{G} = \begin{bmatrix} 0 & \gamma e^{-i3\phi} & 0 \\ \gamma e^{i3\phi} & 0 & 0 \\ 0 & 0 & 0 \end{bmatrix}, \quad \text{(B2c)}$$

where $\phi = k_x a$.

The above equations give the boundary condition between either side of the grain boundary which reads

$$\begin{bmatrix} \mathbf{B}(1) \\ \mathbf{A}(1) \end{bmatrix} = \mathbb{M}_1.\mathbb{M}_2\begin{bmatrix} \mathbf{B}(-1) \\ \mathbf{A}(-1) \end{bmatrix}, \quad \text{(B3)}$$

where the $\mathbb{N}_i$ are 6×6 matrices that read

$$\mathbb{M}_1 = \begin{bmatrix} \frac{\epsilon}{t}\mathcal{P} - W_A^\dagger & \frac{\epsilon}{t}\mathcal{Q} \\ -\mathcal{P} & -\mathcal{Q} \end{bmatrix}, \quad \text{(B4a)}$$

$$\mathbb{M}_2 = \begin{bmatrix} \mathcal{Q}^{-1}\left(\frac{\epsilon}{t}\mathcal{P}W_A^{-1} - W_A^\dagger\right) & \mathcal{Q}^{-1}\mathcal{P}W_A^{-1} \\ -\frac{\epsilon}{t}W_A^{-1} & -W_A^{-1} \end{bmatrix}. \quad \text{(B4b)}$$

In Eqs. (B4) we have used the following definitions for the matrices $\mathcal{P}$ and $\mathcal{Q}$:

$$\mathcal{P} = \frac{\epsilon}{t}\mathbb{I}_3 - \mathcal{X}^T\mathcal{R}, \quad \text{(B5a)}$$

$$\mathcal{Q} = \mathcal{B} + \mathcal{X}^T\mathcal{R}, \quad \text{(B5b)}$$

where $\mathbb{I}_3$ stands for the 3×3 identity matrix, while the matrix $\mathcal{R}$ reads

$$\mathcal{R} = -\frac{1}{\xi^2}\begin{bmatrix} \epsilon & 0 & e^{-3i\phi}\gamma \\ 0 & -\frac{\xi^2}{\beta} & 0 \\ e^{3i\phi}\gamma & 0 & \epsilon \end{bmatrix}. \quad \text{(B6)}$$

Note that the above matrices depend on the reduced energy ϵ/t, the longitudinal momentum k_x, and the hopping parameters at the defect, ξ, γ, and β. Similarly, the boundary condition connecting the two sides of the defect, i.e., $\mathbf{L}(1) = \mathbb{M}_{7557}\cdot\mathbf{L}(-1)$, reads

$$\mathbb{M}_{7557} = R\cdot\ \mathbb{M}_1\cdot\mathbb{M}_2\cdot\ R^T, \quad \text{(B7)}$$

and in general depends on ξ, γ, β, ϵ/t, and k_x.

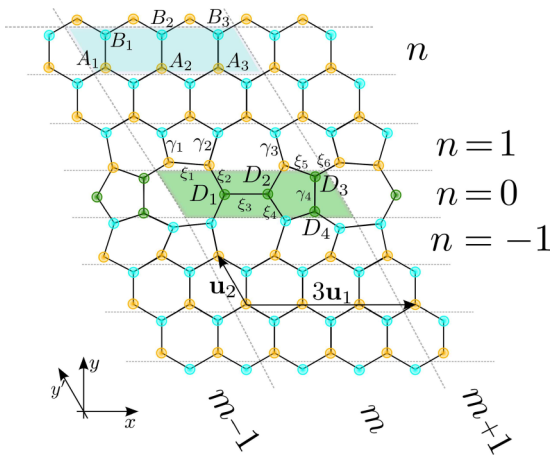

FIG. 16. (Color online) Crystalline structure of the $t7t5$ defect line [32]. The region of the defect line is highlighted in blue.

2. Boundary condition of the $t7t5$ grain boundary

In Fig. 16 we can see the scheme of the crystalline structure of a $t7t5$ grain boundary. In what follows we will compute the boundary condition matrix relating the wave-function amplitudes on either of its sides. For such a grain boundary, the tight-binding equations in the defect region read

$$-\frac{\epsilon}{t}\mathbf{A}(2) = W_A^\dagger \mathbf{B}(1) + \mathbf{B}(2) \tag{B8a}$$

$$-\frac{\epsilon}{t}\mathbf{B}(1) = G_+\mathbf{A}(1) + W_A\mathbf{A}(2), \tag{B8b}$$

$$-\frac{\epsilon}{t}\mathbf{A}(1) = G_+\mathbf{B}(1) + X_1\mathbf{A}(1) + X_2\mathbf{D}, \tag{B8c}$$

$$-\frac{\epsilon}{t}\mathbf{D} = X_2^\dagger\mathbf{A}(1) + \mathcal{S}\mathbf{D} + X_3\mathbf{B}(-1), \tag{B8d}$$

$$-\frac{\epsilon}{t}\mathbf{B}(-1) = G_-\mathbf{A}(-1) + X_3^{\mathrm{T}}\mathbf{D} + X_4\mathbf{B}(-1), \tag{B8e}$$

$$-\frac{\epsilon}{t}\mathbf{A}(-1) = G_-\mathbf{B}(-1) + W_A^\dagger\mathbf{B}(-2), \tag{B8f}$$

where, once more we use the notation $\mathbf{Z}(n) = [Z_1(n), Z_2(n), Z_3(n)]^T$, now for $Z = A, B, D$. The $G_\pm$ are diagonal matrices that can be written as $G_+ = \mathrm{diag}[\gamma_1, \gamma_2, \gamma_3]$ and $G_- = \mathrm{diag}[\gamma_2, \gamma_3, \gamma_1]$, while the X_i matrices (with $i = 1,2,3,4$) read

$$X_1 = \xi_1 \begin{bmatrix} 0 & 1 & 0 \\ 1 & 0 & 0 \\ 0 & 0 & 0 \end{bmatrix}, \tag{B9}$$

$$X_2 = \begin{bmatrix} 0 & 0 & \xi_6 e^{-i3\phi} & 0 \\ \xi_2 & 0 & 0 & 0 \\ 0 & \xi_4 & \xi_5 & 0 \end{bmatrix}, \tag{B10}$$

$$X_3 = \begin{bmatrix} \xi_2 & 0 & 0 \\ 0 & \xi_4 & 0 \\ 0 & 0 & 0 \\ 0 & \xi_5 & \xi_6 \end{bmatrix}, \tag{B11}$$

$$X_4 = \xi_1 \begin{bmatrix} 0 & 0 & e^{-i3\phi} \\ 0 & 0 & 0 \\ e^{i3\phi} & 0 & 0 \end{bmatrix}, \tag{B12}$$

where again $\phi = k_x a$. Finally, $\mathcal{S}$ reads

$$\mathcal{S} = \begin{bmatrix} 0 & \xi_3 & 0 & 0 \\ \xi_3 & 0 & 0 & 0 \\ 0 & 0 & 0 & \xi_4 \\ 0 & 0 & \xi_4 & 0 \end{bmatrix}. \tag{B13}$$

We can rewrite the above equations in a more compact form that allows us to write the equation relating the amplitudes at each side of the grain boundary (i.e., those at $n = 2$ with those at $n = -2$) in the following way:

$$\begin{bmatrix} \mathbf{B}(2) \\ \mathbf{A}(2) \end{bmatrix} = \mathbb{N}_1.\mathbb{N}_2.\mathbb{N}_3.\mathbb{N}_4.\mathbb{N}_5.\mathbb{N}_6 \begin{bmatrix} \mathbf{B}(-2) \\ \mathbf{A}(-2) \end{bmatrix}, \tag{B14}$$

where the matrices $\mathbb{N}_i$ are now 6×6 reading

$$\mathbb{N}_1 = -\begin{bmatrix} \frac{\epsilon}{t}\mathbb{I}_3 & (W_A)^\dagger \\ -\mathbb{I}_3 & 0 \end{bmatrix}, \tag{B15a}$$

$$\mathbb{N}_2 = -\begin{bmatrix} \frac{\epsilon}{t}(W_A)^{-1} & (W_A)^{-1}G_+ \\ -\mathbb{I}_3 & 0 \end{bmatrix}, \tag{B15b}$$

$$\mathbb{N}_3 = -\begin{bmatrix} G_+^{-1}F_1 & G_+^{-1}X_2P^{-1}X_3 \\ -\mathbb{I}_3 & 0 \end{bmatrix}, \tag{B15c}$$

and

$$\mathbb{N}_4 = -\begin{bmatrix} Q^{-1}F_2 & Q^{-1}G_-^{-1} \\ -\mathbb{I}_3 & 0 \end{bmatrix}, \tag{B15d}$$

$$\mathbb{N}_5 = -\begin{bmatrix} \frac{\epsilon}{t}G_-^{-1} & G_-^{-1}(W_A)^\dagger \\ -\mathbb{I}_3 & 0 \end{bmatrix}, \tag{B15e}$$

$$\mathbb{N}_6 = -\begin{bmatrix} \frac{\epsilon}{t}W_A^{-1} & W_A^{-1} \\ -\mathbb{I}_3 & 0 \end{bmatrix}, \tag{B15f}$$

where we have used the following definitions:

$$F_1 = \frac{\epsilon}{t}\mathbb{I}_3 + X_1 + X_2P^{-1}X_2^\dagger, \tag{B16a}$$

$$F_2 = \frac{\epsilon}{t}\mathbb{I}_3 + X_3^{\mathrm{T}}P^{-1}X_3 + X_4, \tag{B16b}$$

$$P = -\frac{\epsilon}{t}\mathbb{I}_3 - \mathcal{S}, \tag{B16c}$$

$$Q = X_3^{\mathrm{T}}P^{-1}X_2^\dagger. \tag{B16d}$$

The above matrices depend on the reduced energy ϵ/t, the longitudinal momentum k_x, and the hopping parameters at the defect, ξ_i and γ_j (with $i = 1,\ldots,6$ and $j = 1,\ldots,4$).

It is now straightforward to write the boundary condition connecting the two sides of the defect $\mathbf{L}(1) = \mathbb{M}_{t7t5} \cdot \mathbf{L}(-1)$, where the boundary condition matrix $\mathbb{M}$ is a 6×6 matrix

given by

$$\mathbb{M}_{t7t5} = R \cdot \mathbb{N}_1 \cdot \mathbb{N}_2 \cdot \mathbb{N}_3 \cdot \mathbb{N}_4 \cdot \mathbb{N}_5 \cdot \mathbb{N}_6 \cdot R^T, \quad \text{(B17)}$$

where, for the sake of simplicity of notation, we have omitted the dependence of the matrices $\mathbb{M}_{t7t5}$ and $\mathbb{N}_i$ on ϵ/t, k_x, ξ_i, and γ_j.

[1] X. Li, W. Cai, J. An, S. Kim, J. Nah, D. Yang, R. Piner, A. Velamakanni, I. Jung, E. Tutuc, S. K. Banerjee, L. Colombo, and R. S. Ruoff, Science **324**, 1312 (2009).

[2] A. Reina, X. Jia, J. Ho, D. Nezich, H. Son, V. Bulovic, M. S. Dresselhaus, and J. Kong, Nano Lett. **9**, 30 (2009).

[3] K. S. Kim, Y. Zhao, H. Jang, S. Y. Lee, J. M. Kim, K. S. Kim, J.-H. Ahn, P. Kim, J.-Y. Choi, and B. H. Hong, Nature (London) **457**, 706 (2009).

[4] S. Bae, H. Kim, Y. Lee, X. Xu, J.-S. Park, Y. Zheng, J. Balakrishnan, T. Lei, H. Ri Kim, Y. I. Song, Y.-J. Kim, K. S. Kim, B. Ozyilmaz, J.-H. Ahn, B. H. Hong, and S. Iijima, Nat. Nanotechnol. **5**, 574 (2010).

[5] J. C. Meyer, C. Kisielowski, R. Erni, M. D. Rossell, M. F. Crommie, and A. Zettl, Nano Lett. **8**, 3582 (2008).

[6] J. Lahiri, Y. Lin, P. Bozkurt, I. I. Oleynik, and M. Batzill, Nat. Nanotechnol. **5**, 326 (2010).

[7] Y. H. Pinshane, C. S. Ruiz-Vargas, A. M. van der Zande, W. S. Whitney, M. P. Levendorf, J. W. Kevek, S. Garg, J. S. Alden, C. J. Hustedt, Y. Zhu, J. Park, P. L. McEuen, and D. A. Muller, Nature (London) **469**, 389 (2011).

[8] K. Kim, Z. Lee, W. Regan, C. Kisielowski, M. F. Crommie, and A. Zettl, ACS Nano **5**, 2142 (2011).

[9] P. Nemes-Incze, K. J. Yoo, L. Tapaszto, G. Dobrik, J. Labar, Z. E. Horvath, C. Hwang, and L. P. Biro, Appl. Phys. Lett. **99**, 023104 (2011).

[10] P. Avouris and C. Dimitrakopoulos, Mater. Today **15**, 86 (2012).

[11] G. Fiori, F. Bonaccorso, G. Iannaccone, T. Palacios, D. Neumaier, A. Seabaugh, S. K. Banerjee, and L. Colombo, Nat. Nano. **9**, 768 (2014).

[12] A. W. Tsen, L. Brown, M. P. Levendorf, F. Ghahari, P. Y. Huang, R. W. Havener, C. S. Ruiz-Vargas, D. A. Muller, P. Kim, and J. Park, Science **336**, 1143 (2012).

[13] B. Yang, H. Xu, J. Lu, and K. P. Loh, J. Am. Chem. Soc. **136**, 12041 (2014).

[14] Y. Tison, J. Lagoute, V. Repain, C. Chacon, Y. Girard, F. Joucken, R. Sporken, F. Gargiulo, O. V. Yazyev, and S. Rousset, Nano Lett. **14**, 6382 (2014).

[15] O. V. Yazyev and Y. P. Chen, Nat. Nano **9**, 755 (2014).

[16] D. Gunlycke and C. T. White, Phys. Rev. Lett. **106**, 136806 (2011).

[17] A. Ayuela, W. Jasklski, H. Santos, and L. Chico, New J. Phys. **16**, 083018 (2014).

[18] J. N. B. Rodrigues, N. M. R. Peres, and J. M. B. L. dos Santos, J. Phys.: Condens. Matter **25**, 075303 (2013).

[19] J. N. B. Rodrigues, N. M. R. Peres, and J. M. B. Lopes dos Santos, Phys. Rev. B **86**, 214206 (2012).

[20] D. Gunlycke and C. T. White, Phys. Rev. B **90**, 035452 (2014).

[21] J.-H. Chen, G. Autès, N. Alem, F. Gargiulo, A. Gautam, M. Linck, C. Kisielowski, O. V. Yazyev, S. G. Louie, and A. Zettl, Phys. Rev. B **89**, 121407 (2014).

[22] S. Malola, H. Häkkinen, and P. Koskinen, Phys. Rev. B **81**, 165447 (2010).

[23] Y. Liu and B. I. Yakobson, Nano Lett. **10**, 2178 (2010).

[24] O. V. Yazyev and S. G. Louie, Phys. Rev. B **81**, 195420 (2010).

[25] O. V. Yazyev and S. G. Louie, Nat. Mater. **9**, 806 (2010).

[26] R. Grantab, V. B. Shenoy, and R. S. Ruoff, Science **330**, 946 (2011).

[27] L. Jiang, X. Lv, and Y. Zheng, Phys. Lett. A **376**, 136 (2011).

[28] L. Jiang, G. Yu, W. Gao, Z. Liu, and Y. Zheng, Phys. Rev. B **86**, 165433 (2012).

[29] Q. Yu, L. A. Jauregui, W. Wu, R. Colby, J. Tian, Z. Su, H. Cao, Z. Liu, D. Pandey, D. Wei, T. F. Chung, P. Peng, N. P. Guisinger, E. A. Stach, J. Bao, S.-S. Pei, and Y. P. Chen, Nat. Mater. **10**, 443 (2011).

[30] L. A. Jauregui, H. Cao, W. Wu, Q. Yu, and Y. P. Chen, Solid State Commun. **151**, 1100 (2011).

[31] J. W. González, H. Santos, M. Pacheco, L. Chico, and L. Brey, Phys. Rev. B **81**, 195406 (2010).

[32] A. R. Botello-Mendez, X. Declerck, M. Terrones, H. Terrones, and J.-C. Charlier, Nanoscale **3**, 2868 (2011).

[33] N. Ansari, F. Nazari, and F. Illas, Phys. Chem. Chem. Phys. **16**, 21473 (2014).

[34] A. B. Kuzmenko, I. Crassee, D. van der Marel, P. Blake, and K. S. Novoselov, Phys. Rev. B **80**, 165406 (2009).

[35] J. Song, H. Liu, H. Jiang, Q.-f. Sun, and X. C. Xie, Phys. Rev. B **86**, 085437 (2012).

[36] D. A. Bahamon, A. L. C. Pereira, and P. A. Schulz, Phys. Rev. B **83**, 155436 (2011).

[37] S. Okada, T. Kawai, and K. Nakada, J. Phys. Soc. Jpn. **80**, 013709 (2011).

[38] L. Kou, C. Tang, W. Guo, and C. Chen, ACS Nano **5**, 1012 (2011).

[39] S. Ihnatsenka and I. V. Zozoulenko, Phys. Rev. B **88**, 085436 (2013).

[40] S. Datta, *Electronic Transport in Mesoscopic Systems* (Cambridge University Press, Cambridge, England, 1999).

[41] M. P. L. Sancho, J. M. L. Sancho, J. M. L. Sancho, and J. Rubio, J. Phys. F: Met. Phys. **15**, 851 (1985).

[42] A.-P. J. H. Haug, *Quantum Kinetics in Transport and Optics of Semiconductors* (Springer, Berlin, 2008).

[43] J. Martin, N. Akerman, G. Ulbricht, T. Lohmann, J. H. Smet, K. von Klitzing, and A. Yacoby, Nat. Phys. **4**, 144 (2008).

[44] Y. Zhang, V. W. Brar, C. Girit, A. Zettl, and M. F. Crommie, Nat. Phys. **5**, 722 (2009).

[45] A. Deshpande, W. Bao, F. Miao, C. N. Lau, and B. J. LeRoy, Phys. Rev. B **79**, 205411 (2009).

[46] E. Rossi, S. Adam, and S. Das Sarma, Phys. Rev. B **79**, 245423 (2009).

[47] J. Wilhelm, M. Walz, and F. Evers, Phys. Rev. B **89**, 195406 (2014).

[48] P. Vancs, G. I. Mrk, P. Lambin, A. Mayer, C. Hwang, and L. P. Bir, Appl. Surf. Sci. **291**, 58 (2014).

[49] P. Vancs, G. I. Mrk, P. Lambin, A. Mayer, Y.-S. Kim, C. Hwang, and L. P. Bir, Carbon **64**, 101 (2013).

[50] E. V. Castro, K. S. Novoselov, S. V. Morozov, N. M. R. Peres, J. M. B. L. dos Santos, J. Nilsson, F. Guinea, A. K. Geim, and A. H. C. Neto, J. Phys.: Condens. Matter **22**, 175503 (2010).
[51] C. J. Páez, D. A. Bahamon, and A. L. C. Pereira, Phys. Rev. B **90**, 125426 (2014).
[52] E. McCann, Phys. Rev. B **74**, 161403 (2006).
[53] M. Koshino and T. Ando, Phys. Rev. B **73**, 245403 (2006).
[54] M. S. Tang, C. Z. Wang, C. T. Chan, and K. M. Ho, Phys. Rev. B **53**, 979 (1996).